Available online at www.sciencedirect.com
SCIENCE DIRECT®
Journal of Computational Physics 202 (2005) 1–19
JOURNAL OF COMPUTATIONAL PHYSICS
www.elsevier.com/locate/jcp

Three-dimensional numerical simulation of flows with complex geometries in a regular Cartesian grid and its application to blood flow in cerebral artery with multiple aneurysms

Kensuke Yokoi [a,b,*], Feng Xiao [c], Hao Liu [d], Kazuaki Fukasaku [e]

[a] *Computer and Information Division, RIKEN (The Institute of Physical and Chemical Research), Wako Saitama 351-0198, Japan*
[b] *Department of Engineering Science and Ocean Engineering, National Taiwan University, Taipei 106, Taiwan*
[c] *Department of Energy Sciences, Tokyo Institute of Technology, Yokohama 226-8502, Japan*
[d] *Department of Electronics and Mechanical Engineering, Chiba University, Yayoi, Chiba 263-8522, Japan*
[e] *Department of Neurosurgery, Kasukabe Central General Hospital, Kasukabe, Saitama 344-0063, Japan*

Received 13 October 2003; received in revised form 4 June 2004; accepted 6 June 2004
Available online 13 August 2004

Abstract

We propose a numerical algorithm to compute flows in a complex geometry such as a blood vessel. The algorithm is based on the level set method, the fractional step method, the CIP method and the ghost fluid method in a regular Cartesian grid. The algorithm was applied to various test problems to verify the reliability of method, and numerical results show that the present method can deal with flows in complex geometries such as a bifurcation and multiple aneurysms robustly.

PACS: 02.70.Bf; 46.15.−x; 83.85.Pt; 95.75.Pq
Keywords: Level set method; CIP method; Ghost fluid method; Complex geometry; Blood flow; Multiple aneurysms

1. Introduction

Fluid phenomena associated with complex structures appear in many places. Examples are biological fluid flows in the human body and multi-phase flows in manufacturing processes. Studies on these fluid flow phenomena are considered challenging but important in various fields such as physics, industry and

* Corresponding author.
E-mail address: kensuke@ntu.edu.tw (K. Yokoi).

0021-9991/$ - see front matter © 2004 Elsevier Inc. All rights reserved.
doi:10.1016/j.jcp.2004.06.018

medicine. Numerical simulation is becoming an effective means for solving such complicated flows, but problems concerning appropriate treatment of complex boundaries as well as boundary conditions remain. In the present paper, we propose a numerical algorithm for overcoming these problems.

As one application of our algorithm, we tried to simulate blood flow in cerebral arteries with multiple aneurysms and a bifurcation as shown in Fig. 1. Although it is well known that vascular diseases may significantly depend on the nature of blood flow [3], the details on its mechanisms are still not so clear.

This is because blood flow, particularly that within the human body, is difficult to measure accurately even using the most developed medical equipments such as magnetic resonance imaging (MRI) and computerized tomography (CT) on a propose of determining the local influence of fluid mechanical factors such as wall-shear stress on the vascular disease.

Numerical simulations of blood flows have been done by using various numerical methods and in coordinate systems with an unstructured grid, a boundary-fitted grid and a regular Cartesian grid. The finite element method based on an unstructured grid has been used widely in recent years [21,22], and this method shows great potential for simulations of fluid flows with complex structures because the mesh can be generated along the surface. However, mesh generation may become difficult in some cases with complex geometries and generally the efficiency of computation such as computer time may be worse than that in the case of the methods using a structured grid. Numerical simulation using the finite volume method with boundary-fitted coordinate (BFC) has also been used widely [11]. Although this method must be the best method for the shapes to be able to generate the BFC, it may not be suitable for flows with complex geometries as illustrated in Fig. 1, such as cerebral arteries with complicated multiple aneurysms. On the other hand, in the methods using a regular Cartesian grid, shapes of the structures are expressed by using particles, density function and level set function. In general, when a regular Cartesian grid is used, the accuracy in expression of the shape is worse than that when using other methods. However, as advantages of a method using a regular Cartesian grid, mesh generation is not required and the computational efficiency is better than that of an unstructured grid-based method. Early works on blood flow simulation using a regular Cartesian grid were carried out by using the immersed boundary method [16]. The immersed boundary method has been applied to some blood flow problems such as flows in a heart. The immersed boundary method is a skillful method that imposes a velocity boundary condition between the fluid and solid through an external force term.

In the present paper, we propose an algorithm based on the regular Cartesian grid in which the velocity boundary conditions on a solid are naturally imposed through a viscosity term and the pressure boundary conditions on the solid surface are determined through a pressure Poisson equation by introducing an open

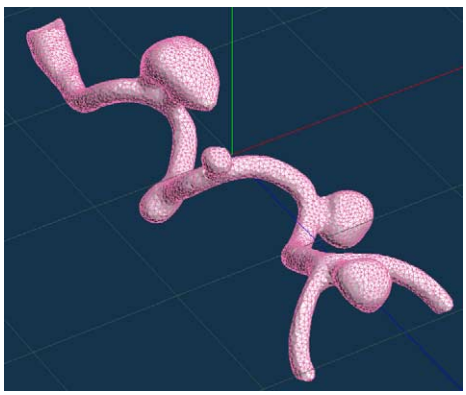

Fig. 1. Model of a cerebral artery with five aneurysms based on medical images.

area ratio. A detailed description of the numerical method is given in Section 2. Four test problems are presented and discussed in Section 3. Medical image processing method is described in Section 4, application of the method to blood flows is described in Section 5, and a short summary is presented in Section 6.

2. Numerical method

The numerical algorithm is based on the fractional step method [9], the cubic interpolated propagation (CIP) method [27,28,2,29], the level set method [14,19,18,15], and the ghost fluid method [6,25,33]. The fractional step method is based on a pressure Poisson equation as used in the MAC method [7] and the projection method [4]. In this paper, we modify this method by introducing an open area ratio to take into account the sub-grid information of the interface within each cell Cartesian grid. The CIP method is of a third-order solver of the advection equation. The level set method is used to capture the interface in a Cartesian grid system. The ghost fluid method is used for implementing a velocity boundary condition on a solid body surface. A staggered grid as shown in Fig. 2 is used. We describe the main aspects of our numerical algorithm in the following sections.

2.1. Governing equations

Blood fluid is considered to be an incompressible and Newtonian fluid. The governing equations can be written as

$$\nabla \cdot \mathbf{u} = 0, \tag{1}$$

$$\frac{\partial \mathbf{u}}{\partial t} + (\mathbf{u} \cdot \nabla)\mathbf{u} = -\frac{\nabla p}{\rho} + \frac{\nabla \cdot \tau}{\rho}, \tag{2}$$

where $\mathbf{u}$ is the velocity, p is the pressure, ρ is the density and τ is the viscous stress tensor. The blood vessel is treated as being rigid because the elastic deformation of the large arteries including cerebral artery is generally less than 10% and the influence is second order for the main blood flow [21].

2.2. Solutions to the governing equations

The governing equations are solved by using the fractional step method. In this method, a fractional step approach on time is used as follows:

$$\mathbf{u}^{t+\nabla t} = A^{\mathrm{NA2}}(A^{\mathrm{NA1}}(A^{\mathrm{A}}\mathbf{u}^{t})). \tag{3}$$

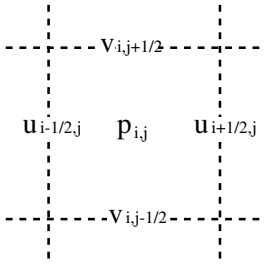

Fig. 2. A staggered grid in two-dimensional case.

Here A^{A}, A^{NA1} and A^{NA2} represent the operators of difference schemes for the advection step, non-advection step 1 and non-advection step 2, respectively, as below:

(1) Advection step (A^{A}):

$$\frac{\partial \mathbf{u}}{\partial t} + (\mathbf{u}\cdot\nabla)\mathbf{u} = 0. \tag{4}$$

(2) Non-advection step 1 (A^{NA1}):

$$\frac{\partial \mathbf{u}}{\partial t} = \frac{\nabla\cdot\tau}{\rho}. \tag{5}$$

(3) Non-advection step 2 (A^{NA2}):

$$\nabla\cdot\mathbf{u} = 0, \tag{6}$$

$$\frac{\partial \mathbf{u}}{\partial t} = -\frac{\nabla p}{\rho}. \tag{7}$$

2.2.1. Advection step

The advection step is calculated by the CIP method. The CIP method is a less-diffusive and stable algorithm for solving the advection equation

$$\frac{\partial f}{\partial t} + (\mathbf{u}\cdot\nabla)f = 0. \tag{8}$$

In a one-dimensional case, the spatial profile between neighboring cells of f is approximated with a cubic interpolated function

$$F_i(x) = a_i(x-x_i)^3 + b_i(x-x_i)^2 + f_i'(x-x_i) + f_i, \tag{9}$$

where f' is $\partial f/\partial x$. From given f_i and f_i', the coefficients a_i and b_i can be determined by imposing the continuities of $F(x)$ and $\partial F(x)/\partial x$ between adjacent cells (see [27] for details). From $F_i(x)$, $f_i^{t+\Delta t}$ can be obtained by shifting the interpolated function as

$$f_i^{t+\Delta t} = F_i(x_i - u_i\Delta t). \tag{10}$$

$\partial f_i^{t+\Delta t}/\partial x$ can be also calculated in a similar way. The interpolation function of f_i' can be obtained as the spatial derivative of F_i:

$$\frac{\partial F_i(x)}{\partial x} \equiv F_i'(x) = 3a_i(x-x_i)^2 + 2b_i(x-x_i) + f_i'. \tag{11}$$

The time evolution equation for f' is actually obtained by taking the spatial differentiation of Eq. (8) with respect to x,

$$\frac{\partial f'}{\partial t} + u\frac{\partial f'}{\partial x} = -f'\frac{\partial u}{\partial x}. \tag{12}$$

The fractional time step method is also applied for Eq. (12). The equation is separated into advection and non-advection parts, and is calculated as

$$\frac{\partial f'}{\partial t} = -F_i'(x_i - u_i\Delta t)\frac{\partial u}{\partial x}. \tag{13}$$

This method can be extended easily to two- and three-dimensional cases [28,2].

2.2.2. Non-advection step

Non-advection step 1 is solved by using the second-order finite difference method and the ghost fluid method (details are given in Section 2.4.),

$$\frac{\mathbf{u}^{**}-\mathbf{u}^{*}}{\Delta t}=\frac{\nabla\cdot\tau}{\rho}, \tag{14}$$

where the superscript $\mathbf{u}^{*}$ denotes the velocity after the calculations for the advection step.

Non-advection step 2 is computed by a method based on a pressure Poisson equation. To take into account the effect of the solid interface in a mesh, we introduce the open area ratio A, which means the fraction of fluid as shown in Fig. 3. The term A can be approximately estimated from the level set function.

The pressure Poisson equation

$$\nabla\cdot\left(A\frac{\nabla p^{t+\Delta t}}{\rho}\right)=\frac{\nabla\cdot A\mathbf{u}^{**}}{\Delta t} \tag{15}$$

can be obtained from Eqs. (6) and (7) by taking into account A. The pressure Poisson equation, which is discretized by a central difference, is computed by the Bi-CGSTAB method [24] with the tridiagonal approximation factorization preconditioner [5]. For consistency with Eq. (15), Eqs. (6) and (7) must be modified as

$$\nabla\cdot A\mathbf{u}^{n+1}=0, \tag{16}$$

$$\frac{\mathbf{u}^{t+\Delta t}-\mathbf{u}^{**}}{\Delta t}=-\frac{A}{A+\epsilon}\frac{\nabla p^{t+\Delta t}}{\rho}, \tag{17}$$

where ϵ is a small positive constant. Eq. (17) is derived from combining Eq. (15) with (16):

$$\nabla\cdot\left\{A\frac{\mathbf{u}^{n+1}-\mathbf{u}^{**}}{\Delta t}\right\}=\nabla\cdot\left\{A\left(-\frac{\nabla p^{t+\Delta t}}{\rho}\right)\right\}. \tag{18}$$

In a two-dimensional case, $\nabla\cdot A\mathbf{u}$ is calculated as

$$\nabla\cdot A\mathbf{u}=\frac{A_{i+\frac{1}{2},j}u_{i+\frac{1}{2},j}-A_{i-\frac{1}{2},j}u_{i-\frac{1}{2},j}}{\Delta x}+\frac{A_{i,j+\frac{1}{2}}v_{i,j+\frac{1}{2}}-A_{i,j-\frac{1}{2}}v_{i,j-\frac{1}{2}}}{\Delta y}. \tag{19}$$

In the present formulation, a pressure boundary condition that maintains continuity across the solid interface is satisfied automatically.

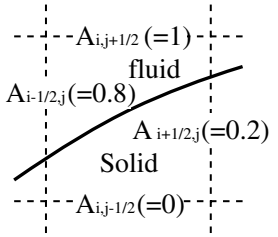

Fig. 3. Schematic figure of open area ratio in two-dimensional case.

2.3. Treatment of the interface

The interface between blood and the blood vessel is captured by the level set method. The level set method is an interface-capturing method and has been applied to various fluid problems with interfaces [18,15,30–32]. This method expresses the surface of an $N-1$ dimension as a zero level (or contour) of an N-dimensional level set function ψ. The signed distance function

$$\begin{aligned} &\psi = 0 \text{ at the interface,} \\ &|\nabla\psi| = 1 \text{ for the whole region,} \end{aligned} \tag{20}$$

is widely used as the level set function (Fig. 4).

Advantages of the level set method are that it can express a smooth curve in a Cartesian grid and can also treat complex geometries such as bifurcations of blood vessels and aneurysms without complicated treatments. The unit normal is always well defined from the level set function

$$n = \frac{\nabla\psi}{|\nabla\psi|}. \tag{21}$$

The unit normal is useful for detecting the location of the interface by using the distance function. These properties play an important role in capturing a flat interface in a Cartesian grid and in implementing the ghost fluid method for boundary conditions on the solid object.

The density (color) function ϕ (Fig. 4), which is used to define the physical properties of different materials, can be generated as a smoothed Heaviside function

$$\phi = H_\alpha(\psi), \tag{22}$$

for instance

$$H_\alpha(\psi) = \begin{cases} 0 & \text{if } \psi < -\alpha, \\ \frac{1}{2}\left[1 + \frac{\psi}{\alpha} + \frac{1}{\pi}\sin\left(\frac{\pi\psi}{\alpha}\right)\right] & \text{if } |\psi| \leqslant \alpha, \\ 1 & \text{if } \psi > \alpha, \end{cases} \tag{23}$$

where 2α represents the distance of the transition region between the fluid region and the solid region. In this paper, we used $2\alpha = 1$.

2.4. Velocity boundary condition at the blood and vessel interface

To impose a no-slip boundary condition on the blood vessel, we use the ghost fluid method. The ghost fluid method is simple and effective for implementing a boundary condition on a solid body in a finite difference framework. In this method, imaginary cells called ghost cells are placed within a few grids from the

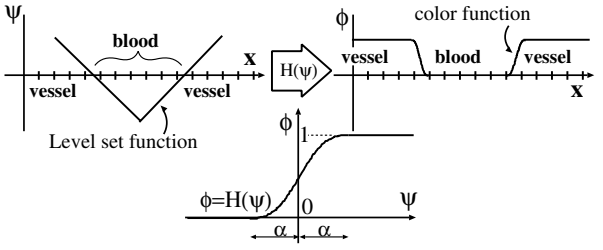

Fig. 4. Schematic figure of level set function and color function.

interface in the solid region. The variables of fluid near the interface are extrapolated into the ghost cells to satisfy the boundary condition on the solid surface.

To impose a no-slip condition on the solid interface, the reverse velocity for flow is put on the ghost cell, such as the method introduced in the MAC method [7] as shown in Figs. 5 and 6. The reverse velocity u_{ghost} on the ghost cells is estimated by a linear extrapolation using the level set function as follows:

$$\mathbf{u}_{\text{ghost}} = \frac{\psi_{\text{ghost}}}{\psi_{\text{blood}}}\mathbf{u}_{\text{blood}}, \tag{24}$$

where u_{blood} is the velocity in the blood as shown in Figs. 5 and 6. ψ_{ghost} is the level set function at the position where $\mathbf{u}_{\text{ghost}}$ is defined. From the definition of Eq. (24), the order of accuracy of the velocity boundary condition is first order. In this study, we used $\psi_{\text{blood}} = \mp\Delta x$, where the "−" sign is used for $\psi_{\text{blood}} < 0$ and "+" is used for $\psi_{\text{blood}} > 0$. $\mathbf{u}_{\text{blood}}$ is derived by solving the advection equation

$$\frac{\partial \mathbf{u}}{\partial t_{\text{g}}} \pm \mathbf{n}\cdot\nabla\mathbf{u} = 0, \tag{25}$$

where the "+" sign is used for $\psi_{\text{ghost}} > 0$, "−" is used for $\psi_{\text{ghost}} < 0$, and t_{g} is an artificial time, in this case $\Delta t_{\text{g}} = |\psi_{\text{ghost}}| + |\psi_{\text{blood}}|$.

To solve Eq. (25) we use a semi-Lagrangian approach because $|\mathbf{n}\Delta t_{\text{g}}|$ is usually larger than Δx (i.e., CFL number > 1) as shown in Fig. 6. We use a first-order semi-Lagrangian scheme. Although we also tried a high-order semi-Lagrangian scheme based on the CIP method [20], there was no significant difference in the results. Therefore, the first-order scheme seems to be sufficient for the calculation of Eq. (25).

In the first-order semi-Lagrangian formulation, the interpolation function is constructed using the grid points surrounding the position where $\mathbf{u}_{\text{blood}}$ is defined, marked by the black circles as shown in Fig. 6. In a three-dimensional case, we use the following interpolation function:

$$F(x,y,z) = a_{111}XYZ + a_{110}XY + a_{011}YZ + a_{101}ZX + f_xX + f_yY + f_zZ + f_{i',j',k'}, \tag{26}$$

$$X = x - x_{i',j',k'}, \quad Y = y - y_{i',j',k'}, \quad Z = z - z_{i',j',k'}, \tag{27}$$

$$f_x = \frac{f_{iup',j',k'} - f_{i',j',k'}}{\Delta x}, \tag{28}$$

$$f_y = \frac{f_{i',jup',k'} - f_{i',j',k'}}{\Delta y}, \tag{29}$$

$$f_z = \frac{f_{i',j',kup'} - f_{i',j',k'}}{\Delta z}, \tag{30}$$

$$a_{110} = \frac{f_{iup',jup',k'} - f_{i',j',k'}}{\Delta x\Delta y} - \frac{f_x\Delta x + f_y\Delta y}{\Delta x\Delta y}, \tag{31}$$

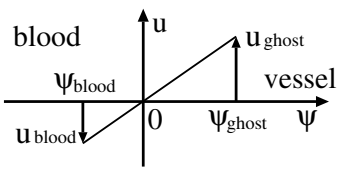

Fig. 5. Schematic figure of the ghost fluid method.

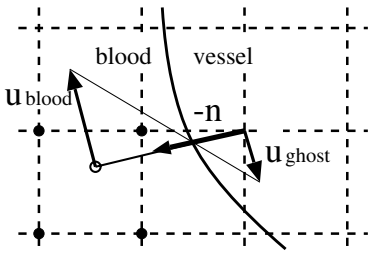

Fig. 6. Another view of Fig. 5. The curve represents the solid interface. This is for $\psi_{\text{ghost}} > 0$. If $\psi_{\text{ghost}} < 0$, replace $-\mathbf{n}$ to $\mathbf{n}$.

$$a_{011} = \frac{f_{i',jup',kup'} - f_{i',j',k'}}{\Delta y \Delta z} - \frac{f_y \Delta y + f_z \Delta z}{\Delta y \Delta z}, \tag{32}$$

$$a_{101} = \frac{f_{iup',j',kup'} - f_{i',j',k'}}{\Delta x \Delta z} - \frac{f_x \Delta x + f_z \Delta z}{\Delta x \Delta z}, \tag{33}$$

$$a_{111} = \frac{f_{iup',jup',kup'} - f_{i',j',k'}}{\Delta x \Delta y \Delta z} - \frac{a_{110}\Delta x \Delta y + a_{011}\Delta y \Delta z + a_{101}\Delta x \Delta z}{\Delta x \Delta y \Delta z} - \frac{f_x \Delta x + f_y \Delta y + f_z \Delta z}{\Delta x \Delta y \Delta z},$$

here $i' = i + \text{int}(-n_x \Delta t_g/|\Delta x|)$, $iup' = i' + \text{sign}(-n_x \Delta t_g)$, $\Delta x = x_{iup',j'} - x_{i',j'}$, int($a$) denotes the integer part of a. $\mathbf{u}_{\text{fluid}}$ can be computed from $F(x_{i,j,k} - n_x \Delta t_g, y_{i,j,k} - n_y \Delta t_g, z_{i,j,k} - n_z \Delta t_g)$ or $F(x_{i',j',k'} - \text{mod}(n_x \Delta t_g/|\Delta x|), y_{i',j',k'} - \text{mod}(n_y \Delta t_g/|\Delta y|), z_{i',j',k'} - \text{mod}(n_z \Delta t_g/|\Delta z|))$, where mod($a/b$) means the reminder of a/b.

3. Test problems

To verify the present numerical method, we carried out a series of simulations of a three-dimensional Poiseuille flow, a Womersley problem (pulsatile three-dimensional Poiseuille flow), a two-dimensional Couette flow, and flow around a circular cylinder.

3.1. Three-dimensional Poiseuille flow

Fig. 7 shows a configuration of Poiseuille flow. The shape of the tube is defined with the level set function analytically and the shape is represented well in a Cartesian fixed grid. The theoretical solution is

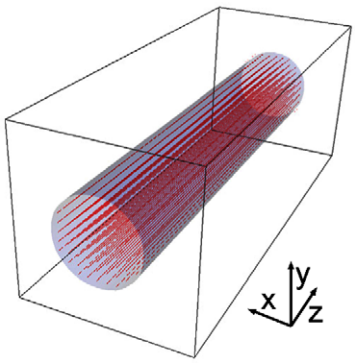

Fig. 7. The configuration and vector field of three-dimensional Poiseuille's flow.

$$u_z = \frac{1}{4\mu}\left(-\frac{\mathrm{d}p}{\mathrm{d}z}\right)(a^2 - r^2), \tag{34}$$

where a is the radius of the tube. Fig. 8 shows a comparison of velocity profiles between the numerical and the theoretical solutions. The computed velocity profiles agree well with the analytical solution, even though the diameter of the tube is covered by only 11.2 grids. If GFM is not implemented (i.e., $\mathbf{u}_{\mathrm{ghost}} = 0$), it is difficult to use the method for flow problems with a boundary layer such as blood flow as shown in Fig. 8. This is because the reverse velocity at the ghost cells is not predicted.

Convergence study is performed for the problem. In this study, three grid sizes (Δx = 1.0, 0.5, 0.25 mm) are used. Fig. 9 shows the spatial distribution of errors. The error is defined as $\sqrt{(u_i^{\mathrm{sim}} - u_i^{\mathrm{exact}})^2}$, where u_{sim} and u_{exact} are the velocities of the simulation and the exact solution, respectively. The errors near the cylinder surface are dominant. This is because the linear extrapolation is used to estimate the velocity on the ghost cell. Actually a second-order extrapolation should be use for the problem because the analytical velocity distribution Eq. (8) is given by a quadratic function. Therefore, in the problem the velocity of the simulation is slightly greater than the velocity of the exact solution.

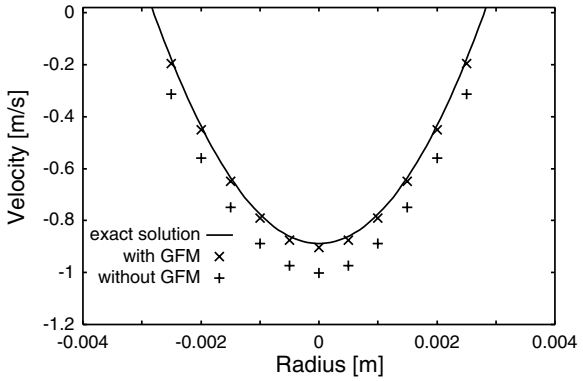

Fig. 8. Comparison between the numerical results with/without GFM and the theoretical velocity profile. The dots and lines represent the numerical and theoretical solutions, respectively. $\mu = 4.9 \times 10^{-3}$ Pa s and the radius of a tube 2.8 mm are used. The Reynolds number is 536. The Cartesian grid of $\Delta x = \Delta y = \Delta z = 0.5$ mm is used.

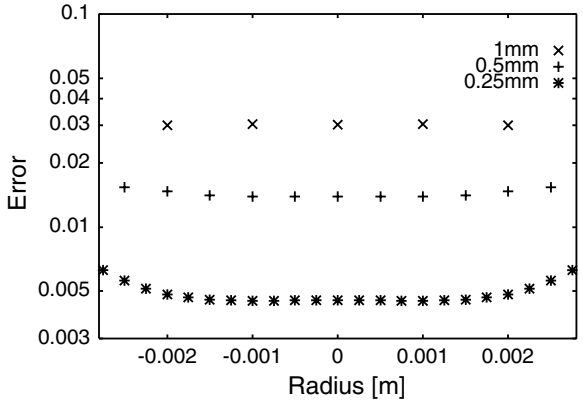

Fig. 9. Spatial distributions of error for each resolution.

Table 1
Errors and convergence rates ($Re = 536$)

	1.0 mm	Rate	0.5 mm	Rate	0.25 mm
L_2	1.35×10^{-2}	1.64	4.34×10^{-3}	2.14	9.83×10^{-4}
L_∞	3.04×10^{-2}	0.98	1.54×10^{-2}	1.29	6.29×10^{-3}

L_2 and L_∞ are shown in Table 1. L_2 and L_∞ are defined as

$$L_2 = \frac{1}{N}\sqrt{\sum_{i=1}^{N}(u_i^{\mathrm{sim}} - u_i^{\mathrm{exact}})^2}, \tag{35}$$

$$L_\infty = \max |u_i^{\mathrm{sim}} - u_i^{\mathrm{exact}}|. \tag{36}$$

The results show that the method is first order at the solid interface and 1.5-order in most of the domain.

Convergence study for a higher Reynolds number ($Re = 1072$) was also carried out, and the results are shown in Table 2. From Tables 1 and 2, we can know that these errors are proportional to the Reynolds number. This means that the relative error does not change. This is consistent with the analytical solution (34), which is proportional to the Reynolds number.

3.2. Velocity profile of a pulsatile flow

To further validate the time accuracy, we applied the present method to a pulsatile Poiseuille flow problem that has an exact solution called a Womersley solution [26,13]. The configuration is the same as that for the Poiseuille problem except that the pressure gradient $\mathrm{d}p/\mathrm{d}z$ is pulsatile:

$$\frac{\mathrm{d}p}{\mathrm{d}z} = C\mathrm{e}^{\mathrm{i}\omega t}, \tag{37}$$

where C is a constant and i is the imaginary number. Then, the velocity profile has the analytical solution

$$u(r) = \frac{\mathrm{i}C}{\rho\omega}\left[1 - \frac{J_0(\alpha^{r/a}\mathrm{i}^{3/2})}{J_0(\alpha\mathrm{i}^{3/2})}\right], \tag{38}$$

where a is the radius of the tube, α is the Womersley number and J_0 is the Bessel function of the first kind of order zero. A comparison of computed and analytical solutions shows that they have good agreement as shown in Fig. 10. Resolution study was also performed for the problem as shown in Fig. 11. Even in just five grids, the velocity profile is captured well. Table 3 shows L_2 and L_∞ norms of the error. In the problem, error estimation was difficult because the numerical errors counteract each other by the cyclic movement.

3.3. Two-dimensional Couette flow

To check the influence of the Cartesian grid on flows with a circular geometry, the method was applied to a Couette flow problem. The configuration of the Couette flow is shown in Fig. 12. A liquid is poured in a cylinder that rotates with a constant angular velocity ω_{cyli}. The theoretical solution of the velocity profile is

Table 2
Errors and convergence rates ($Re = 1072$)

	1.0 mm	Rate	0.5 mm	Rate	0.25 mm
L_2	2.65×10^{-2}	1.63	8.57×10^{-3}	2.08	2.02×10^{-3}
L_∞	5.93×10^{-2}	0.95	3.07×10^{-2}	1.28	1.26×10^{-2}

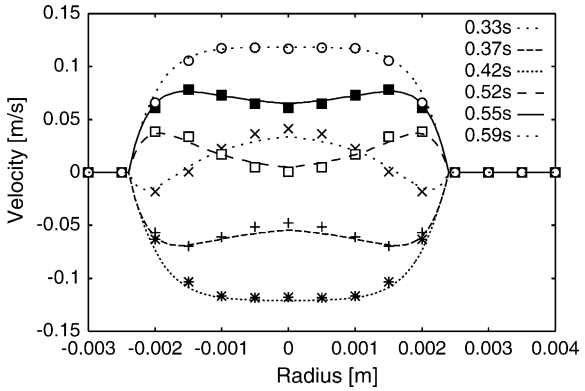

Fig. 10. Comparison of velocity profiles between numerical and theoretical results. Each line represents the analytic solution at an instant ($Re = 120$ and $\alpha = 4.72$).

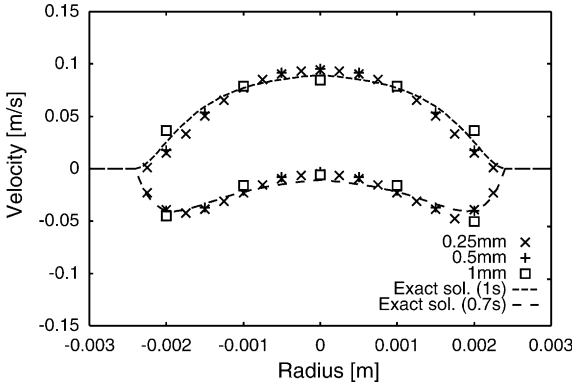

Fig. 11. Comparison of velocity profiles between numerical and theoretical results at $t = 0.7$ and 1.0 s with the different resolutions $\Delta x = 1.0, 0.5, 0.25$ mm.

Table 3
Errors for Womersley problem at 1 s

	1.0 mm	0.5 mm	0.25 mm
L_2	3.27×10^{-3}	1.93×10^{-3}	1.55×10^{-3}
L_∞	1.10×10^{-2}	7.81×10^{-3}	1.14 x 10^{-2}

$$v(r) = \omega_{\text{cyli}} r, \tag{39}$$

where r is the radius. Rotation of the tube is expressed at the ghost grids. To deal with a moving solid object, Eq. (24) is modified as follows:

$$\mathbf{u}_{\text{ghost}} = \frac{\psi_{\text{ghost}}}{\psi_{\text{blood}}} \mathbf{u}_{\text{blood}} + \left(1 - \frac{\psi_{\text{ghost}}}{\psi_{\text{blood}}}\right) \mathbf{u}_{\text{surf}}, \tag{40}$$

where $\mathbf{u}_{\text{surf}}$ is the velocity at the solid surface. In this problem, $\mathbf{u}_{\text{surf}}$ is given as

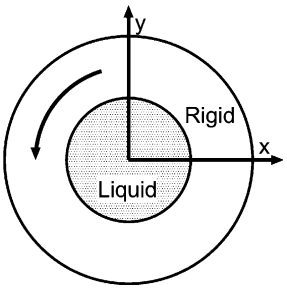

Fig. 12. Configuration of a Couette flow.

$$u_{\mathrm{surf},x} = -\omega_{\mathrm{cyli}} y_{\mathrm{cyli}} = -\omega_{\mathrm{cyli}} r_{\mathrm{cyli}} n_y, \tag{41}$$

$$u_{\mathrm{surf},y} = -\omega_{\mathrm{cyli}} x_{\mathrm{cyli}} = -\omega_{\mathrm{cyli}} r_{\mathrm{cyli}} n_x, \tag{42}$$

Here, we assumed $\psi_{\mathrm{ghost}} > 0$. If $\psi_{\mathrm{ghost}} < 0$, n_x and n_y are replaced by $-n_x$ and $-n_y$. Fig. 13 shows a comparison of numerical and theoretical results. The dots denote the y-component of the velocity on the x-axis. The results show that the model can treat well a circular shape with a small number of Cartesian grid points.

Table 4 shows the results of the convergence study. Some fluctuation in the convergence rate, especially between 0.5 and 1.0 mm was observed. It was found that the fraction of the open area has a significant effect on the numerical solution and that a more uniform convergence rate could be obtained if the computations for all levels were conducted with the same fraction for the open area.

3.4. Two-dimensional flow past a circular cylinder

We also applied the present method to simulate flows past a circular cylinder. In this simulation, the cylinder diameter is represented by 9.4 grids. Fig. 14 shows a snapshot of the vorticity contours at a dimensionless time $T = 185$, where T is defined as $u_\infty t/D$, u_∞ is the velocity at the incoming boundary and D is the diameter of the cylinder. In the simulation, $u_\infty = 1$ and $D = 1$ were used. The Karman vortex street was detected.

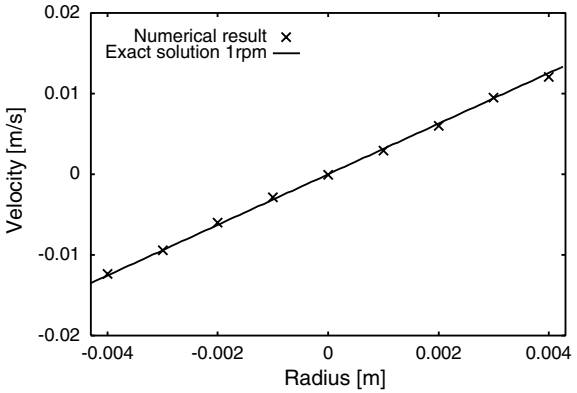

Fig. 13. The dots and lines represent the numerical and theoretical solutions. As the radius of the cylinder, 4.3 mm is used. The viscosity coefficient is $\mu = 4.9 \times 10^{-3}$ Pa s and the angular velocity $\omega_{\mathrm{cyli}} = 1$ rpm. The Cartesian grid of $\Delta x = \Delta y = 1$ mm is used.

Table 4
Convergence study for Couette flow problem

	2.0 mm	Rate	1.0 mm	Rate	0.5 mm	Rate	0.25 mm
L_2	2.60×10^{-4}	1.62	8.48×10^{-5}	0.75	5.04×10^{-5}	1.69	1.56×10^{-5}
L_∞	1.03×10^{-3}	1.05	4.96×10^{-4}	0.35	3.89×10^{-4}	1.42	1.45×10^{-4}

Fig. 14. Vorticity contour of the flow around a circular cylinder at $Re = 200$.

Fig. 15 shows the time history of the drag coefficient C_D and the lift coefficient C_L, C_D and C_L are defined as

$$C_D = \frac{F_D}{(1/2)\rho u_\infty^2 D}, \quad C_L = \frac{F_L}{(1/2)\rho u_\infty^2 D}, \tag{43}$$

where F_D is the drag force, F_L the lift force and $\rho = 1$. The Strouhal number St is measured as

$$St = \frac{fD}{u_\infty}, \tag{44}$$

where f is the vortex shedding frequency. Table 5 shows a comparison of the computed values of C_D, C_L and St and the experimental results [10,17]. It seems that the present results show reasonable agreement even with such a coarse grid.

Numerical simulations for different values of Re were performed, and the results are shown in Table 6. A Karmen vortex street appears from $Re = 50$.

These results agree well with the experiment results. Resolution studies were also conducted for $Re = 40$ and $Re = 200$. It seems that C_D approaches to the experimental results as resolution increases.

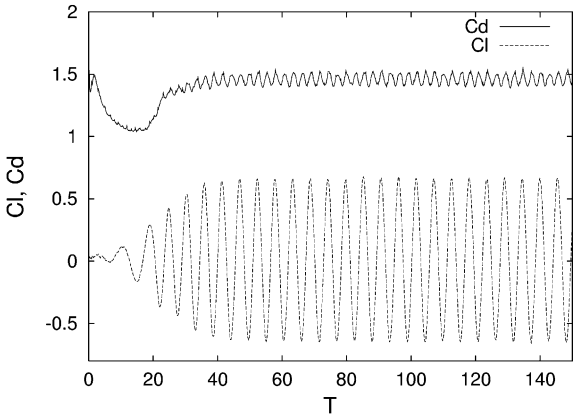

Fig. 15. The time history of C_D and C_L at $Re = 200$.

Table 5
Comparison of C_D, C_L and St with computations and measurements

	C_D	C_L	St
Present	1.46 ± 0.05	±0.66	0.182
Liu et al.	1.31 ± 0.049	±0.69	0.192
Rogers et al.	1.23 ± 0.05	±0.65	0.185
Rosenfield et al.	1.46 ± 0.04	±0.69	0.211
Roshko (exp.)	–	–	0.19
Wille (exp.)	1.30	–	–

Table 6
C_D for some Reynolds numbers and computations with a measurement, and resolution study for $Re = 40$ and $Re = 200$

Re	Present			Tritton (exp.) [23]
	450×300	300×150	150×75	
10		3.04		
20		2.16		2.22
40	1.50	1.57	1.81	1.48
50		1.47		
100		1.40		
200	1.28	1.46	1.58	

4. Medical image processing

As a pre-processing step for fluid computations, these is a need to construct a computational geometric model based on medical image data. We constructed a surface model of polygons by using a method such as thresholding and region growing methods [12,18,15]. Software such as Visualization Tool Kit (VTK) [34] may be useful for generating a polygon model. Polygon-based modeling is very convenient for editing the geometry by means of polygon modelers or 3D-CAD such as Metasequoia [35] as shown in Fig. 16. To study the relationship between vessel geometry and blood flow, the geometric model must be modified.

To simulate flow with the geometric model, the level set function is constructed from the polygon data by calculating the shortest distance to polygons. The calculation is sufficient only for a narrow band within Δh (where Δh is the grid spacing) from the interface. To save computational time, it is better to compute other domains by the fast marching method [1,18,37] or an iterative approach [32].

When calculation of only the geometry of the original medical image is required, it is better to use a region growing method based on the level set method [12,18,15] for geometry modeling. This is because the output is the level set function which can be used directly for the flow computation.

5. Blood flow in a cerebral artery

We then applied the method to simulation of blood flow in a cerebral artery with multiple aneurysms as illustrated in Fig. 1. The model is a composite of five separate human aneurysms (i.e., replica), and was made by Kerber [8]. The model was provided in a silicon model as shown in Fig. 17. To implement the shape model in our numerical method, we filled radiopaque dye (contrast agent) in the silicon model and created the volume data by using CT.

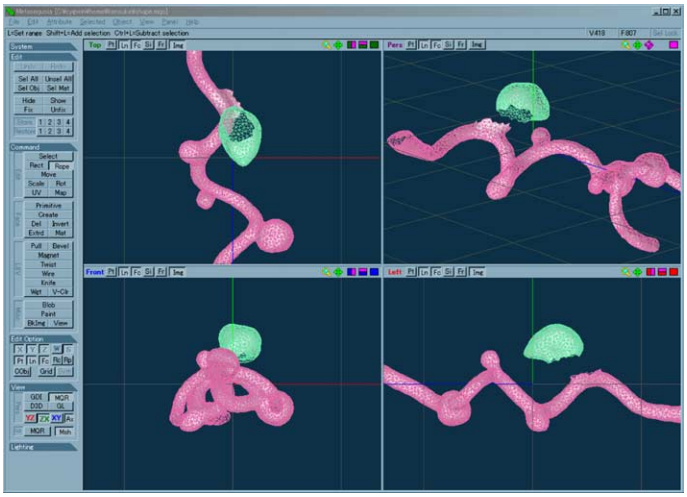

Fig. 16. Demonstration of a polygon modeler, Metasequoia.

Fig. 17. Shape model made by silicon. Courtesy of C.W. Kerber.

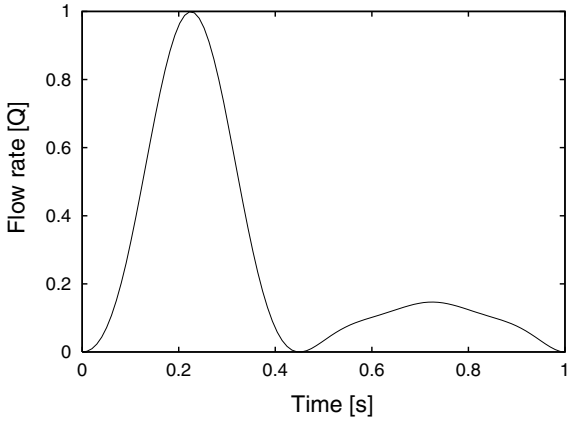

Fig. 18. Incoming flow rate with a physiological waveform.

As inlet boundary condition, a physiological flow rate (Eq. (45) and Fig. 18) introduced by McDonald [13] is used:

$$Q = 0.251 + 0.290(\cos\phi_Q + 0.97\cos 2\phi_Q + 0.47\cos 3\phi_Q + 0.14\cos 4\phi_Q), \tag{45}$$

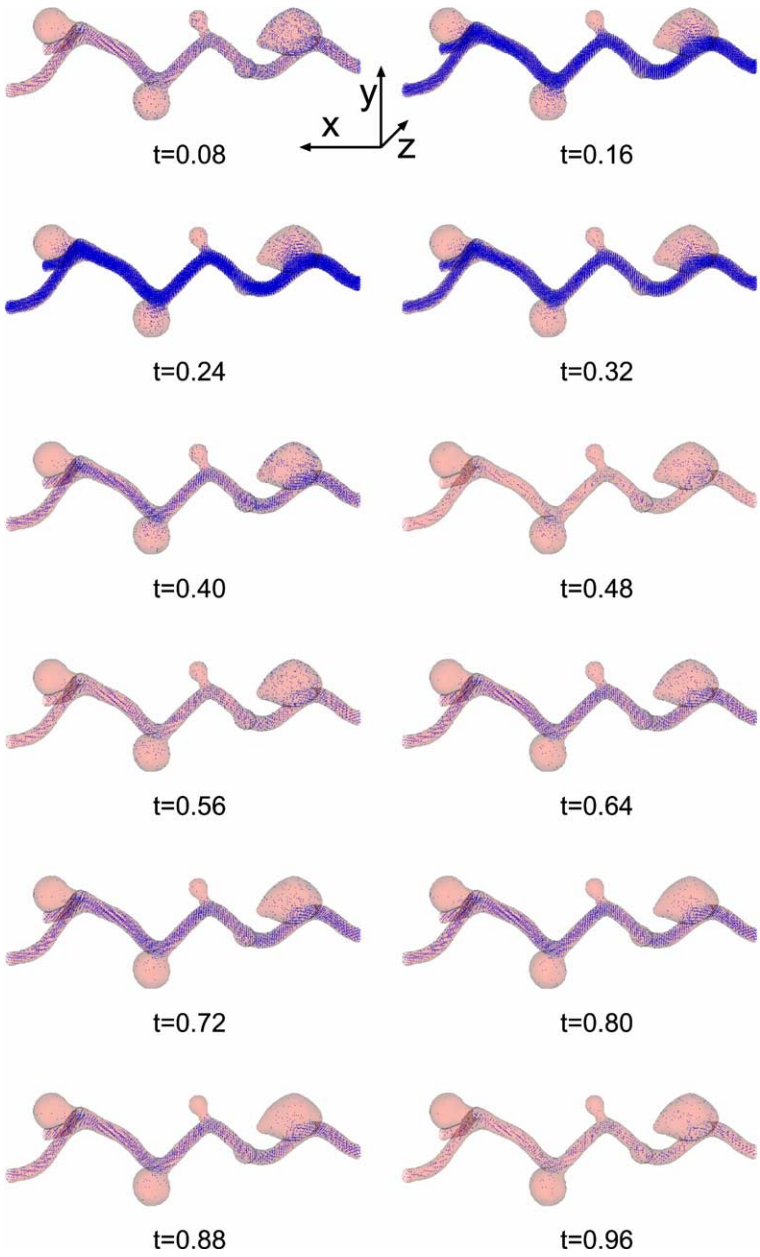

Fig. 19. Time evolution of blood flow in cerebral artery with five aneurysms. The velocity and shape are plotted. The movies are available in [36].

where Q is the volmatic flow rate and $\phi_Q = 2\pi t - 1.4142$. Note that the pulse outputs a minimum flow rate of zero once between the systolic and the distole. The time series of the simulation and streame lines at $t = 0.32$ are shown in Figs. 19 and 20, respectively. In the simulation, $165 \times 70 \times 55$ grids and $Re = 200$ were used. Fig. 21 shows flows around the left most and right most aneurysms. The Reynolds number is defined based on a typical set of medical data associated with the blood flow in the cerebral artery, involv-

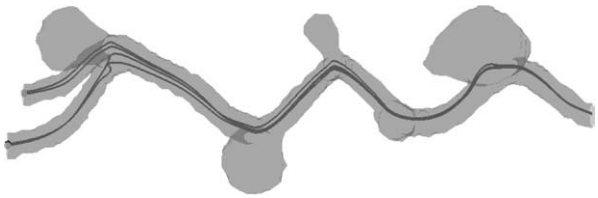

Fig. 20. Streame line at $t = 0.32$.

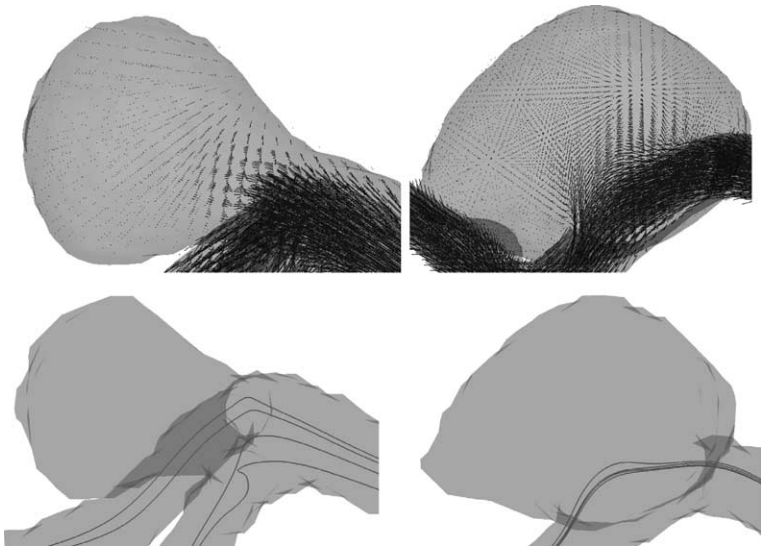

Fig. 21. Snapshots of flows around the left most and right most aneurysms.

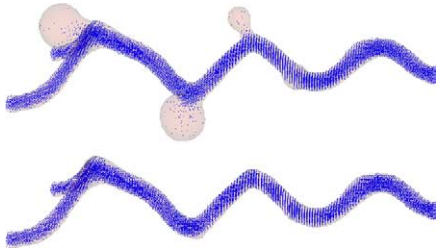

Fig. 22. Snapshots of blood flow with four aneurysms and without aneurysms. The movies are available in [36].

ing a maximum flow rate of 2.0 cm^3/s and a representative diameter of 3.0 mm. The corresponding Womersley number is then calculated to be approximately 1.9. The present method shows robustness in simulating flows in such a complex geometry as well as potential in the simulation for a modified model with the aneurysms cut off as shown in Fig. 22, where the aneurysms were removed artificially by a polygon modeler.

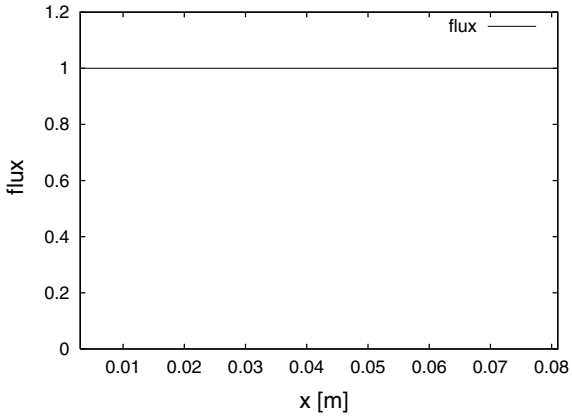

Fig. 23. Flux at $t = 0.32$. The flux has been normalized the incoming flux as 1.

To check up the flux conservation, the flux against x is plotted in Fig. 23. Here the flux is defined as $\int u_x \mathrm{d}y\,\mathrm{d}z$ and u_x is the x component of the velocity. The error ($\mathrm{flux}_{\max} - \mathrm{flux}_{\min}$) is less than 10^{-5} when the convergence tolerance of the pressure Poisson equation $\epsilon = 10^{-10}$ is used. This means that the divergence free is satisfied precisely.

The present study, for the first time, shows the feasibility of computational modeling of unsteady, three-dimensional hemodynamics in a cerebral artery with five aneurysms. We see that the pulsatile blood flows in the cerebral artery with multiple aneurysms are well simulated. Our results demonstrate while large-scale vortices and hence circulations are observed in the aneurysms throughout the stroke cycle, they show comparatively lower velocities and the streamwise flow apparently dominates the blood flow in the aneurysms and the artery, respectively, as shown in Figs. 19, 21 and 22. The influence of the proximal aneurysms to the distal ones is seemingly not an issue. This may show different features due to the variation of the physiological conditions at inlet and outlets, or, in the waveform of the inflow (Fig. 18) [11]. Further quantitative investigation on such kinds of issues is needed.

6. Summary

We have proposed a numerical algorithm for flows in a complex geometry based on the level set method, the fractional step method, the CIP method and the ghost fluid method in a regular Cartesian grid. The validity of the method was checked by test problems of Poiseuille, Couette and Wormersley flows, and the flow around a circular cylinder. Results of simulation of the blood flow in a cerebral artery with multiple aneurysms show that the method can treat flow in complex geometries such as a bifurcation and multiple aneurysms robustly.

Acknowledgements

We thank Kangbin Lei, Masato Ida, Takehiro Himeno and Tony W.H. Sheu for their useful discussions and comments. Numerical computation for this work was carried out at the Computer and Information Division, RIKEN. K.Y. is grateful to RIKEN for support through a Special Postdoctoral fellowship.

References

[1] D. Adalsteinsson, J.A. Sethian, The fast construction of extension velocities in level set methods, J. Comput. Phys. 148 (1999) 2.
[2] T. Aoki, Multi-dimensional advection of CIP (cubic-interpolated propagation) scheme, CFD J. 4 (1995) 279.
[3] J.V. Byrne, G. Guglielmi, Endovascular treatment of intracranial aneurysms, Springer, Berlin, 1998.
[4] A.J. Chorin, Numerical solution of the Navier–Stokes equations, J. Math. Comput. 22 (1968) 745.
[5] S. Doi, N. Harada, Tridiagonal factorization algorithm: a preconditioner for nonsymmetric system solving on vector computers, I. Inform. Proc. 11 (1987) 38.
[6] R. Fedkiw, et al., A non-oscillatory Eulerian approach to interface in multimaterial flows (the ghost fluid method), J. Comput. Phys. 152 (1999) 457.
[7] F.H. Harlow, J.E. Welch, Numerical calculation of time-dependent viscous incompressible flow of fluid with free surface, Phys. Fluid. 8 (1965) 2182.
[8] C.W. Kerber, S.G. Imbesi, K. Knox, Flow dynamics in a lethal anterrior communicating artery aneurysm, AJNR Am. J. Neuroradol. 20 (1999) 2000.
[9] J. Kim, P. Moin, Applications of a fractional step method to incompressible Navier–Stokes equations, J. Comput. Phys. 59 (1985) 308.
[10] C. Liu, X. Zheng, C.H. Sung, Preconditioned multigrid methods for unsteady incompressible flows, J. Comput. Phys. 139 (1998) 35.
[11] H. Liu, T. Yamaguchi, Wave dependence of pulsatile flow in a stenosed channel, ASME J. Biomech. Eng. 123 (2001) 88.
[12] R. Malladi, J.A. Sethian, B.C. Vemuri, Evolutionary Fronts for Topology-independent Shape Modeling and RecoveryLecture Notes in Computer Science, No. 800, vol. 3, Springer, Berlin, 1994.
[13] D.A. McDonald, Blood Flow in Arteries, second ed., Arnold, London, 1974.
[14] S. Osher, J.A. Sethian, Front propagating with curvature-dependent speed: algorithms based on Hamilton–Jacobi formulation, J. Comput. Phys. 79 (1988) 12.
[15] S. Osher, R. Fedkiw, Level Set Methods and Dynamics Implicit SurfaceLecture Notes in Applied Mathematical Sciences, No. 153, vol. 3, Springer, Berlin, 2003.
[16] C.S. Peskin, Numerical analysis of blood flow in the heart, J. Comput. Phys. 25 (1977) 220.
[17] S.E. Rogers, D. Kwak, Upwind differencing scheme for the time-accurate incompressible Navier–Stokes equations, AIAA J. 28 (2) (1990) 253.
[18] J.A. Sethian, Level Set Methods and Fast Marching Methods, Cambridge University Press, Cambridge, 1999.
[19] M. Sussman, P. Smereka, S. Osher, A level set approach for capturing solution to incompressible two-phase flow, J. Comput. Phys. 114 (1994) 146.
[20] K. Sakurai, T. Aoki, T. Yabe, A semi-Lagrangian cubic-interpolated propagation (CIP) scheme for long parcel trajectories, CFD J. 10 (2001) 76.
[21] C. Taylor, et al., Finite element modeling of blood flow in arteries, Comput. Methods Appl. Mech. Eng. 26 (1998) 975.
[22] R. Torii, et al., Numerical simulation system for blood flow in the cerebral artery using CT imaging data, JSME Int. J., Ser. C 44 (2001) 982.
[23] D.J. Tritton, Experiments on the flow past a circular cylinder at low Reynolds number, J. Fluid Mech. 6 (1959) 547.
[24] H.A. van der Vorst, Bi-CGSTAB: a fast and smoothly converging variant of Bi-CG for the solution of nonsymmetric linear systems, SIAM J. Sci. Statist. 13 (1992) 631.
[25] M. Watanabe, R. Kikinis, C.F. Westin, Level Set Based Integration of Segmentation and Computational Fluid Dynamics for Flow Correction in Phase Contrast AngiographyLecture Notes in Computer Science, No. 2489, vol. 405, Springer, Berlin, 2002.
[26] J.R. Womersley, Method for the calculation of velocity rate of flow and viscous drag in arteries when the pressure gradient is known, J. Physiol. 127 (1955) 553.
[27] T. Yabe, T. Aoki, A universal solver for hyperbolic-equation by cubic-polynomial interpolation. I. One-demensional solver, Comput. Phys. Commun. 66 (1991) 219.
[28] T. Yabe, et al., A universal solver for hyperbolic-equation by cubic-polynomial interpolation. II. Two- and three dimensional solvers, Comput. Phys. Commun. 66 (1991) 233.
[29] T. Yabe, F. Xiao, T. Utsumi, The constrained interpolation profile method for multiphase analysis, J. Comput. Phys. 169 (2001) 2.
[30] K. Yokoi, F. Xiao, Relationships between a roller and a dynamic pressure distribution in circular hydraulic jumps, Phys. Rev. E 61 (2000) R1016.
[31] K. Yokoi, F. Xiao, Mechanism of structure formation in circular hydraulic jumps: numerical studies of strongly deformed free surface shallow flows, Physica D 161 (2002) 202.
[32] K. Yokoi, Numerical method for complex moving boundary problems in a Cartesian fixed grid, Phys. Rev. E 65 (2002) 055701(R).
[33] K. Yokoi, Numerical method for moving solid object in flows, Phys. Rev. E 67 (2003) 045701(R).
[34] Available from: <http://public.kitware.com/>.
[35] Available from: <http://www21.ocn.ne.jp/ mizno/main_e.html>.
[36] Available from: <http://www.es.que.jp/kensuke/>.
[37] Y.R. Tsai, Rapid and accurate computation of the distance function using grids, J. Comput. Phys. 178 (2001) 175.